INTERNATIONAL JOURNAL FOR NUMERICAL METHODS IN FLUIDS
Int. J. Numer. Meth. Fluids 2005; **49**:395–416
Published online 3 June 2005 in Wiley InterScience (www.interscience.wiley.com). DOI: 10.1002/fld.1003

An iterative stabilized fractional step algorithm for numerical solution of incompressible N–S equations

Xikui Li*,† and Xianhong Han

State Key Laboratory of Structural Analysis of Industrial Equipment, Dalian University of Technology, Dalian 116023, People's Republic of China

SUMMARY

Stabilized fractional step algorithm has been widely employed for numerical solution of incompressible Navier–Stokes equations. However, smaller time step sizes are required to use for existing explicit and semi-implicit versions of the algorithm due to their fully or partially explicit nature particularly for highly viscous flow problems.

The purpose of this paper is to present two modified versions of the fractional step algorithm using characteristic based split and Taylor–Galerkin like based split. The proposed modified versions of the algorithm are based on introducing an iterative procedure into the algorithm and allow much larger time step sizes than those required to the preceding ones.

A numerical study of stability at acceptable convergence rate and accuracy as well as capability in circumventing the restriction imposed by the LBB condition for the proposed iterative versions of the algorithm is carried out with the plane Poisseuille flow problem under different Reynolds numbers ranging from low to high viscosities. Numerical experiments in the plane Poisseuille flow and the lid-driven cavity flow problems demonstrate the improved performance of the proposed versions of the algorithm, which are further applied to numerical simulation of the polymer injection moulding process.

KEY WORDS: incompressible Navier–Stokes equation; fractional step method; iterative procedure; finite element method; stabilization technique

*Correspondence to: Xikui Li, State Key Laboratory of Structural Analysis of Industrial Equipment, Dalian University of Technology, Dalian 116023, People's Republic of China.
†E-mail: xikuili@dlut.edu.cn

Contract/grant sponsor: National Natural Science Foundation, China; contract/grant numbers: 10272027, 10590354, 50278012
Contract/grant sponsor: National Key Basic Research and Development Program; contract/grant number: 2002CB412709

Received 25 January 2005
Revised 25 April 2005
Accepted 3 May 2005

1. INTRODUCTION

It is known that the fractional step algorithm allows the use of the standard Galerkin approximation for the discretization of Navier–Stokes equations in the spatial domain, on the other hand, the restriction imposed by the LBB condition in the interpolating shape functions $\mathbf{N}_u$ and $\mathbf{N}_p$ for the $\mathbf{u}$–p mixed formulations may be also circumvented by using the algorithm as a stabilization technique.The algorithm is based on introducing a split process in temporal discretization of incompressible N–S equations initially presented independently by Chorin [1, 2] and Temam [3] for incompressible flow problems in the finite difference method. The split process was extended to finite element context by Comini *et al.* [4] and Donea *et al.* [5] followed by many different applications for numerical solutions of incompressible N–S equations.

The explicit (or semi-explicit) form of the algorithm is popular and widely employed in practical engineering computations since its simplicity in programming and economy in computational efforts required for each time step, but at the expense of conditional stability, which implies that the time steps will be inevitably small and a restriction in maximum time step size is imposed to the algorithm.

On the other hand, it was concluded by Guermond *et al.* [6] that the fractional step algorithm can circumvent the restriction imposed by the LBB condition in using the same low order interpolation approximations for velocity and pressure variables in the time-dependent incompressible N–S equations only if the non-incremental version of the algorithm is used with the time step size larger than a critical value. Otherwise severe node-to-node spatial oscillations occur in the resulting pressure field, which implies that a minimum time step size requirement is presented for circumventing the restriction imposed by the LBB condition, and therefore ensuring the stability of the algorithm regarding the use of the same low order interpolations for velocity and pressure variables.

In modelling high-viscosity (low Reynolds number) fluid flows such as molten polymer flow in injection moulding, the maximum time step size allowed for the explicit form of the algorithm decreases with increasing viscosity that reduces the efficiency of the numerical solution procedure. In addition, the maximum time step size limitation will possibly conflict with the minimum time step size requirement described above. Though the limitation in the maximum time step size to the explicit form of the algorithm can be alleviated in the semi-explicit form to some extent, numerical results of test examples, particularly the lid-driven cavity flow problem, given in the present work indicate that the limitation still restrict applications of the algorithm with acceptable efficiency and accuracy. It means that the smaller value of maximum time step size required in the explicit (or the semi-explicit) form will become a choke point in applying the fractional step algorithm particularly in the modelling of high or moderate viscosity fluid flow.

In this paper two modified versions of the fractional step algorithm are proposed for finite element solutions of incompressible N–S equations. It is based on introducing an iterative procedure into the algorithm to make the convective term satisfy the momentum conservation equation in an implicit sense. A similar scheme for introducing the iterative procedure into the stabilized fractional step algorithm has been proposed for finite element analysis in saturated soil dynamics [7], which reduces in a decisive manner the computational effort. The iterative versions of the algorithm proposed in this paper allow much larger time step sizes to be used for the numerical solutions of incompressible N–S equations with different values of the

Reynolds number ranging from low to high viscosities. As a consequence, the minimum time step size requirement imposed by the LBB condition will possibly not become an obstacle to impede the application of the algorithm, particularly in the flow problems with moderate or high viscosities even the proposed versions belong to the category of the incremental (pressure correction) method, which will be demonstrated by the numerical results of the test example given later.

It should be stressed that the iterative procedure introduced into the algorithm will less expend computational efficiency, particularly in view of non-linearity of the non-Newtonian (or even including the visco-elastic effect) flow problems in which an iterative process is essentially required to satisfy the non-linear momentum conservation condition.

Numerical experiments in the plane Poisseuille flow under different Reynolds numbers ranging from low to high viscosities and the lid-driven cavity flow problems demonstrate the improved performance of the proposed versions of the algorithm, which are further applied to numerical simulation of the polymer injection moulding process with high efficiency.

2. GOVERNING EQUATIONS AND CHARACTERISTIC BASED TEMPORAL DISCRETIZATION

Momentum and mass conservation equations for incompressible flow can be written as

$$\rho \frac{\mathrm{D}u_i}{\mathrm{D}t} = \rho \left(\frac{\partial u_i}{\partial t} + \frac{\partial u_i}{\partial x_j} u_j \right) = \frac{\partial \tau_{ij}}{\partial x_j} - \frac{\partial p}{\partial x_i} + \rho g_i \tag{1}$$

$$u_{i,i} = 0 \tag{2}$$

where ρ is the fluid density, ρg_i the body forces, μ the viscosity constant. The velocities u_i and the pressure p are the primitive independent variables. The deviatoric stresses are linked to the strain rates and can be expressed by

$$\tau_{ij} = 2\mu \dot{\varepsilon}_{ij} = \mu \left(\frac{\partial u_i}{\partial x_j} + \frac{\partial u_j}{\partial x_i} \right) \tag{3}$$

for Newtonian flows.

2.1. *Characteristic-Galerkin method and Taylor–Galerkin method*

Before proceeding with the split procedure of the fractional step algorithm, we consider the discretization of Equation (1) in time domain within a typical time sub-interval $[t_n, t_{n+1}]$ with $\Delta t = t_{n+1} - t_n$. With substitution of Equation (3) into Equation (1), the time discretization of Equation (1) along the characteristic gives the form of the characteristic-Galerkin method

as [8]

$$\frac{\rho}{\Delta t}[u_i^{n+1}-u_i^n]=\rho g_i-\rho u_j^{n+1/2}\frac{\partial u_i^n}{\partial x_j}+\frac{\Delta t}{2}\rho\left(\frac{\partial u_i^n}{\partial x_j}u_l^n\frac{\partial u_j^n}{\partial x_l}+\frac{\partial^2 u_i^n}{\partial x_j\partial x_k}u_j^{n+1/2}u_k^{n+1/2}\right)$$
$$+\frac{\partial}{\partial x_j}\left(\mu\left(\frac{\partial u_i^{n+\theta}}{\partial x_j}+\frac{\partial u_j^{n+\theta}}{\partial x_i}\right)\right)-(1-\theta)\Delta t u_k^{n+1/2}\frac{\partial}{\partial x_k}\frac{\partial}{\partial x_j}\left(\mu\left(\frac{\partial u_i^n}{\partial x_j}+\frac{\partial u_j^n}{\partial x_i}\right)\right)$$
$$-\frac{\partial p^{n+\theta}}{\partial x_i}+(1-\theta)\Delta t u_k^{n+1/2}\left(\frac{\partial}{\partial x_k}\frac{\partial p^n}{\partial x_i}\right) \tag{4}$$

in which $u_j^{n+1/2}=(u_j^{n+1}+u_j^n)/2$, $\theta\in[0,1]$ with $\theta=0$ for explicit forms and $0<\theta\leqslant 1$ for semi- and fully-implicit forms and particularly

$$p^{n+\theta}=(1-\theta)p^n+\theta p^{n+1} \tag{5}$$

An auxiliary variable u_i^* is introduced in such a way that the characteristic based split (CBS) of Equation (4) is written in the form as below

$$\frac{\rho}{\Delta t}(u_i^*-u_i^n)-\theta\frac{\partial}{\partial x_j}\left(\mu\left(\frac{\partial(u_i^*-u_i^n)}{\partial x_j}+\frac{\partial(u_j^*-u_j^n)}{\partial x_i}\right)\right)$$
$$=\rho g_i-\rho u_j^{n+1/2}\frac{\partial u_i^n}{\partial x_j}+\frac{\Delta t}{2}\rho\left(\frac{\partial u_i^n}{\partial x_j}u_l^n\frac{\partial u_j^n}{\partial x_l}+\frac{\partial^2 u_i^n}{\partial x_j\partial x_k}u_j^{n+1/2}u_k^{n+1/2}\right)+\frac{\partial}{\partial x_j}\left(\mu\left(\frac{\partial u_i^n}{\partial x_j}+\frac{\partial u_j^n}{\partial x_i}\right)\right)$$
$$-(1-\theta)\Delta t u_k^{n+1/2}\frac{\partial}{\partial x_k}\left(\mu\left(\frac{\partial u_i^n}{\partial x_j}+\frac{\partial u_j^n}{\partial x_i}\right)\right)-\frac{\partial p^n}{\partial x_i}+(1-\theta)\Delta t u_k^{n+1/2}\frac{\partial}{\partial x_k}\left(\frac{\partial p^n}{\partial x_i}\right) \tag{6}$$

$$\frac{\rho}{\Delta t}(u_i^{n+1}-u_i^*)-\theta\frac{\partial}{\partial x_j}\left(\mu\left(\frac{\partial(u_i^{n+1}-u_i^*)}{\partial x_j}+\frac{\partial(u_j^{n+1}-u_j^*)}{\partial x_i}\right)\right)=-\theta\frac{\partial}{\partial x_i}(p^{n+1}-p^n) \tag{7}$$

Equations (6) and (7) can be written in the matrix–vector form as

$$\left(\frac{\rho}{\Delta t}\mathbf{I}_3-\theta\mathbf{S}^{\mathrm{T}}(\mu\mathbf{D}_0)\mathbf{S}\right)(\mathbf{u}^*-\mathbf{u}^n)=\rho\mathbf{g}-\rho\mathbf{u}^{n+1/2}\cdot\nabla\mathbf{u}^n+\mathbf{S}^{\mathrm{T}}(\mu\mathbf{D}_0)\mathbf{S}\mathbf{u}^n-\nabla p^n$$
$$+\frac{\Delta t}{2}\rho[(\mathbf{u}^n\cdot\nabla\mathbf{u}^n)\cdot\nabla\mathbf{u}^n+\mathbf{u}^{n+1/2}\cdot(\mathbf{u}^{n+1/2}\cdot\nabla(\nabla\mathbf{u}^n))]$$
$$-(1-\theta)\Delta t(\mathbf{u}^{n+1/2}\cdot\nabla)\mathbf{S}^{\mathrm{T}}(\mu\mathbf{D}_0)\mathbf{S}\mathbf{u}^n+(1-\theta)\Delta t$$
$$\times(\mathbf{u}^{n+1/2}\cdot\nabla)\nabla p^n \tag{8}$$

$$\left(\frac{\rho}{\Delta t}\mathbf{I}_3-\theta\mathbf{S}^{\mathrm{T}}(\mu\mathbf{D}_0)\mathbf{S}\right)(\mathbf{u}^{n+1}-\mathbf{u}^*)=-\theta\nabla\Delta p \tag{9}$$

with $\mathbf{g}=[g_1\ g_2\ g_3]$, $\Delta p = p^{n+1} - p^n$, $\mathbf{D}_0 = \mathrm{diag}(2\ 2\ 2\ 1\ 1\ 1)$, $\mathbf{I}_3$ the 3×3 identity matrix and $\mathbf{S}$ the strain matrix (operator) linked the strain rates to the velocities and defined for three-dimensional problems by

$$\mathbf{S}^{\mathrm{T}} = \begin{bmatrix} \partial/\partial x_1 & 0 & 0 & \partial/\partial x_2 & 0 & \partial/\partial x_3 \\ 0 & \partial/\partial x_2 & 0 & \partial/\partial x_1 & \partial/\partial x_3 & 0 \\ 0 & 0 & \partial/\partial x_3 & 0 & \partial/\partial x_2 & \partial/\partial x_1 \end{bmatrix} \tag{10}$$

Taking the divergence of the vector equation (9), omitting the high order terms of Equation (9) and substituting the incompressibility condition (2) into Equation (9) results in the Poisson equation for the pressure given as

$$\theta\nabla^2\Delta p = \frac{\rho}{\Delta t}\nabla\cdot\mathbf{u}^* \tag{11}$$

The governing equations can be solved after spatial discretization in three steps:

(1) Solve Equation (8) for $\mathbf{u}^*$ with $\mathbf{u}^{n+1/2}$ taken as a known value, say equal to $\mathbf{u}^n$ in the explicit form.
(2) Obtain Δp from Equation (11) and $p^{n+1} = p^n + \Delta p$.
(3) Use Equation (9) to determine $\mathbf{u}^{n+1}$ once $\mathbf{u}^*$ and Δp are known.

Alternatively Equation (1) can be discretized in time domain by the Taylor–Galerkin based method [9, 10] written in the matrix–vector form

$$\frac{\rho}{\Delta t}(\mathbf{u}^{n+1} - \mathbf{u}^n) = \rho\mathbf{g} - (\rho\mathbf{u}\cdot\nabla\mathbf{u})^{n+\theta} + \mathbf{S}^{\mathrm{T}}(\mu\mathbf{D}_0)\mathbf{S}\mathbf{u}^{n+\theta} - \nabla p^{n+\theta} \tag{12}$$

in which a Crank–Nicolson representation is adopted for both the diffusive terms and the convective terms and which is similar to the temporal discretization of Equation (1) carried out in Reference [10]. The Taylor–Galerkin based split (TGBS) of Equation (12) results in

$$\left(\frac{\rho}{\Delta t}\mathbf{I}_3 - \theta\mathbf{S}^{\mathrm{T}}(\mu\mathbf{D}_0)\mathbf{S}\right)(\mathbf{u}^* - \mathbf{u}^n) = \rho\mathbf{g} - \rho\mathbf{u}^{n+\theta}\cdot\nabla\mathbf{u}^{n+\theta} + \mathbf{S}^{\mathrm{T}}(\mu\mathbf{D}_0)\mathbf{S}\mathbf{u}^n - \nabla p^n \tag{13}$$

Equations (8), (11), (9) and Equations (13), (11), (9) constitute temporally discretized governing equations of the semi-implicit CBS and TGBS schemes, respectively.

2.2. *I-CBS and I-TGBS schemes*

To fulfill the momentum conservation equation for incompressible flow in the implicit sense from the view of both convective and diffusive terms, an iterative procedure is introduced to construct the two versions, named as I-CBS and I-TGBS, of the stabilized fractional step algorithm based on Equations (8), (11), (9) and Equations (13), (11), (9), respectively, as follows:

(1) let $\mathbf{u}_0^{n+1} = \mathbf{u}^n$ and the number of iterations $i \Leftarrow 1$,
(2) compute $\mathbf{u}_i^{n+1/2} = (\mathbf{u}_{i-1}^{n+1} + \mathbf{u}^n)/2$ and use it to solve for $\mathbf{u}_i^*$ by Equation (8) for iterative CBS scheme (I-CBS) or Equation (13) for iterative TGBS (I-TGBS) scheme,
(3) determine Δp_i by the solution of the Poisson equation (11) and obtain $p_i^{n+1} = p^n + \Delta p_i$,

(4) solve Equation (9) to determine $\mathbf{u}_i^{n+1}$ by using $\mathbf{u}_i^*$ and Δp_i,
(5) check for convergence of the ith iteration, if $\|\mathbf{u}_i^{n+1}-\mathbf{u}_{i-1}^{n+1}\|_\infty \leqslant \varepsilon$, terminate the iteration loop, otherwise $i \Leftarrow i+1$ and go to (2).

2.3. Existing CBS and TGBS schemes

Most of existing split schemes for temporal discretization was developed on the characteristic or the Taylor–Galerkin basis. They may be classified into the explicit or the semi-implicit ones with the non-incremental or the incremental form according to if all the pressure gradient terms are removed from Equation (8) at the prediction step and therefore the pressure gradient appears in the non-incremental or the incremental form at Equation (11) (the projection step). Among them, the following three schemes are particularly considered to compare their performances with the two proposed ones:

(1) The CBS scheme, in which all the diffusive (viscous) terms are retained at the right-hand side of Equation (4), while all the pressure gradient terms are removed from Equation (4) [8] (CBS-NE: CBS, Non-incremental, Explicit). The three temporally discretized governing equations for the scheme can be written as

$$\frac{\rho}{\Delta t}(\mathbf{u}^*-\mathbf{u}^n)=\rho\mathbf{g}-\rho\mathbf{u}^n\cdot\nabla\mathbf{u}^n+\mathbf{S}^{\mathrm{T}}(\mu\mathbf{D}_0)\mathbf{S}\mathbf{u}^n+\frac{\Delta t}{2}\rho[(\mathbf{u}^n\cdot\nabla\mathbf{u}^n)\cdot\nabla\mathbf{u}^n +\mathbf{u}^n\cdot(\mathbf{u}^n\cdot\nabla(\nabla\mathbf{u}^n))]-(1-\theta)\Delta t(\mathbf{u}^n\cdot\nabla)\mathbf{S}^{\mathrm{T}}(\mu\mathbf{D}_0)\mathbf{S}\mathbf{u}^n \tag{14}$$

$$\nabla^2 p^{n+\theta}=\frac{\rho}{\Delta t}\nabla\cdot\mathbf{u}^* \tag{15}$$

$$\frac{\rho}{\Delta t}(\mathbf{u}^{n+1}-\mathbf{u}^*)=-\nabla p^{n+\theta}+(1-\theta)\Delta t(\mathbf{u}^n\cdot\nabla)\nabla p^n \tag{16}$$

(2) The CBS scheme, in which all the diffusive (viscous) terms and the pressure gradient term corresponding to t_n are retained at the right-hand side of Equation (4) [9] (CBS-IE: CBS, Incremental, Explicit). The three temporally discretized governing equations for the scheme are written as

$$\begin{aligned}\frac{\rho}{\Delta t}(\mathbf{u}^*-\mathbf{u}^n)=\;&\rho\mathbf{g}-\rho\mathbf{u}^n\cdot\nabla\mathbf{u}^n+\mathbf{S}^{\mathrm{T}}(\mu\mathbf{D}_0)\mathbf{S}\mathbf{u}^n-\nabla p^n\\&+\frac{\Delta t}{2}\rho[(\mathbf{u}^n\cdot\nabla\mathbf{u}^n)\cdot\nabla\mathbf{u}^n+\mathbf{u}^n\cdot(\mathbf{u}^n\cdot\nabla(\nabla\mathbf{u}^n))]\\&-(1-\theta)\Delta t(\mathbf{u}^n\cdot\nabla)\mathbf{S}^{\mathrm{T}}(\mu\mathbf{D}_0)\mathbf{S}\mathbf{u}^n+(1-\theta)\Delta t(\mathbf{u}^n\cdot\nabla)\nabla p^n\end{aligned} \tag{17}$$

$$\theta\nabla^2\Delta p=\frac{\rho}{\Delta t}\nabla\cdot\mathbf{u}^* \tag{18}$$

$$\frac{\rho}{\Delta t}(\mathbf{u}^{n+1}-\mathbf{u}^*)=-\theta\nabla\Delta p \tag{19}$$

(3) The TGBS scheme adopting a Crank–Nicolson representation for the diffusive terms, in which part of the diffusive term is removed to the left-hand side of Equation (4) [10]; (TGBS, incremental, semi-implicit). The three temporally discretized governing

equations for the scheme are written as

$$\left(\frac{\rho}{\Delta t}\mathbf{I}_3 - \theta\mathbf{S}^{\mathrm{T}}(\mu\mathbf{D}_0)\mathbf{S}\right)(\mathbf{u}^* - \mathbf{u}^n) = \rho\mathbf{g} - \rho\mathbf{u}^n \cdot \nabla\mathbf{u}^n + \mathbf{S}^{\mathrm{T}}(\mu\mathbf{D}_0)\mathbf{S}\mathbf{u}^n - \nabla p^n \tag{20}$$

$$\theta\nabla^2\Delta p = \frac{\rho}{\Delta t}\nabla \cdot \mathbf{u}^* \tag{21}$$

$$\left(\frac{\rho}{\Delta t}\mathbf{I}_3 - \theta\mathbf{S}^{\mathrm{T}}(\mu\mathbf{D}_0)\mathbf{S}\right)(\mathbf{u}^{n+1} - \mathbf{u}^*) = -\theta\nabla\Delta p \tag{22}$$

3. SPATIAL DISCRETIZATION AND SOLUTION PROCEDURE

The fractional step algorithm performs time discretization before the spatial discretization. The primitive unknown variables u_i, p are spatially approximated using standard finite element shape functions $\mathbf{N}_u, \mathbf{N}_p$ and expressed in terms of their nodal values $\bar{\mathbf{u}}_i, \bar{\mathbf{p}}$ as

$$u_i = \mathbf{N}_u\bar{\mathbf{u}}_i, \quad p = \mathbf{N}_p\bar{\mathbf{p}} \tag{23}$$

By using the standard Galerkin procedure, the weak forms of Equations (8), (11), (9) along with the weak forms of corresponding natural boundary conditions, respectively, can be written as

$$\left(\frac{\rho}{\Delta t}\mathbf{M} + \theta\mathbf{K}_{\mathbf{u}} - \theta\mathbf{K}_u^{\Gamma}\right)(\bar{\mathbf{u}}^* - \bar{\mathbf{u}}^n) = -\rho\mathbf{C}\bar{\mathbf{u}}^n - \mathbf{K}_{\mathbf{u}}\bar{\mathbf{u}}^n + \mathbf{L}^{\mathrm{T}}\bar{\mathbf{p}}^n + \mathbf{f}_s - \rho\frac{\Delta t}{2}(\mathbf{C}_1 - \mathbf{C}_2)\bar{\mathbf{u}}^n + (1-\theta)\Delta t\mathbf{K}_{\mathbf{u}2}\bar{\mathbf{u}}^n - (1-\theta)\Delta t\mathbf{L}_2\bar{\mathbf{p}}^n \tag{24}$$

$$\theta\mathbf{K}_p\Delta\bar{\mathbf{p}} = -\frac{\rho}{\Delta t}\mathbf{L}\bar{\mathbf{u}}^* + \mathbf{f}_p \tag{25}$$

$$\left(\frac{\rho}{\Delta t}\mathbf{M} + \theta\mathbf{K}_{\mathbf{u}} - \theta\mathbf{K}_u^{\Gamma}\right)(\bar{\mathbf{u}}^{n+1} - \bar{\mathbf{u}}^*) = \theta\mathbf{L}^{\mathrm{T}}\Delta\bar{\mathbf{p}} \tag{26}$$

which can be in turn used to solve for nodal values $\bar{\mathbf{u}}^*, \Delta\bar{\mathbf{p}}, \bar{\mathbf{u}}^{n+1}$. The matrices and vectors arising in Equations (24)–(26) are given as

$$\begin{aligned}
\mathbf{M} &= \int_\Omega \mathbf{N}_{\mathbf{u}}^{\mathrm{T}}\mathbf{N}_{\mathbf{u}}\,\mathrm{d}\Omega, & \mathbf{K}_{\mathbf{u}} &= \int_\Omega (\mathbf{S}\mathbf{N}_{\mathbf{u}})^{\mathrm{T}}\mu\mathbf{D}_0\mathbf{S}\mathbf{N}_{\mathbf{u}}\,\mathrm{d}\Omega \\
\mathbf{K}_p &= \int_\Omega (\nabla\mathbf{N}_p)^{\mathrm{T}}(\nabla\mathbf{N}_p)\,\mathrm{d}\Omega, & \mathbf{C} &= \int_\Omega \mathbf{N}_{\mathrm{u}}^{\mathrm{T}}(\mathbf{u}^{n+1/2}\cdot\nabla)\mathbf{N}_{\mathbf{u}}\,\mathrm{d}\Omega \\
\mathbf{C}_1 &= \int_\Omega \frac{\partial}{\partial x_k}(u_k^{n+1/2}u_j^{n+1/2}\mathbf{N}_{\mathrm{u}}^{\mathrm{T}})\frac{\partial\mathbf{N}_{\mathbf{u}}}{\partial x_j}\,\mathrm{d}\Omega, & \mathbf{C}_2 &= \int_\Omega \mathbf{N}_{\mathrm{u}}^{\mathrm{T}}u_l^n\frac{\partial u_j^n}{\partial x_l}\frac{\partial\mathbf{N}_{\mathbf{u}}}{\partial x_j}\,\mathrm{d}\Omega \\
\mathbf{L} &= \int_\Omega \mathbf{N}_p^{\mathrm{T}}(\nabla\cdot\mathbf{N}_{\mathbf{u}})\,\mathrm{d}\Omega, & \mathbf{L}_2 &= \int_\Omega \frac{\partial}{\partial x_k}(u_k^{n+1/2}\mathbf{N}_{\mathrm{u}}^{\mathrm{T}})(\nabla\mathbf{N}_p)\,\mathrm{d}\Omega \\
\mathbf{K}_{\mathbf{u}2} &= \int_\Omega \frac{\partial}{\partial x_k}(u_k^{n+1/2}\mathbf{N}_{\mathrm{u}}^{\mathrm{T}})\mathbf{S}^{\mathrm{T}}(\mu\mathbf{D}_0)\mathbf{S}\mathbf{N}_{\mathbf{u}}\,\mathrm{d}\Omega
\end{aligned} \tag{27}$$

$$\mathbf{K}_u^{\Gamma} = \int_{\Gamma} \mathbf{N}_{\mathrm{u}}^{\mathrm{T}} \mathbf{n}_2 (\mu \mathbf{D}_0) \mathbf{S} \mathbf{N}_{\mathbf{u}} \, \mathrm{d}\Gamma \tag{28}$$

$$\mathbf{f}_s = \int_{\Omega} \mathbf{N}_{\mathbf{u}}^{\mathrm{T}} \rho \mathbf{g} \, \mathrm{d}\Omega + \int_{\Gamma} \mathbf{N}_{\mathbf{u}}^{\mathrm{T}} \bar{\mathbf{t}}^n \, \mathrm{d}\Gamma - \frac{\Delta t}{2} \int_{\Gamma} \mathbf{N}_{\mathbf{u}}^{\mathrm{T}} u_k^{n+1/2} n_k \rho \mathbf{u}_t^n \, \mathrm{d}\Gamma$$

$$\cong \int_{\Omega} \mathbf{N}_{\mathbf{u}}^{\mathrm{T}} \rho \mathbf{g} \, \mathrm{d}\Omega + \int_{\Gamma_t} \mathbf{N}_{\mathbf{u}}^{\mathrm{T}} \bar{\mathbf{t}}^{n+\theta} \, \mathrm{d}\Gamma \tag{29}$$

$$\mathbf{f}_p = \theta \int_{\Gamma} \mathbf{N}_{\mathrm{p}}^{\mathrm{T}} \mathbf{n}^{\mathrm{T}} \nabla \Delta p \, \mathrm{d}\Gamma \tag{30}$$

with

$$\mathbf{n}_2 = \begin{bmatrix} n_x & 0 & 0 & n_y & 0 & n_z \\ 0 & n_y & 0 & n_x & n_z & 0 \\ 0 & 0 & n_z & 0 & n_y & n_x \end{bmatrix} \quad \mathbf{n}^{\mathrm{T}} = [n_x \ n_y \ n_z] \tag{31}$$

$$\rho \mathbf{u}_t^n = -\rho \mathbf{u}^{n+1/2} \cdot \nabla \mathbf{u}^n + \mathbf{S}^{\mathrm{T}} (\mu \mathbf{D}_0) \mathbf{S} \mathbf{u}^n - \nabla p^n \quad (\theta = \tfrac{1}{2}) \tag{32}$$

where $\bar{\mathbf{t}}^{n+\theta}$ is the traction at the boundaries $\Gamma_t = \Gamma_{tt} + \Gamma_{tc}$ at time $t_{n+\theta}$, directly prescribed by traction boundary conditions at Γ_{tt}, including zero traction in the case of free surfaces of fluids, or determined according to contact conditions of fluids with solid boundaries at Γ_{tc}. It is noted that the terms integrated along the boundaries, generated due to integration by parts and associated with unknown nodal variables $\bar{\mathbf{u}}^*$, $\bar{\mathbf{u}}^{n+1}$ are removed to the left-hand sides of Equations (24) and (26), respectively.

With the omission of the high order terms of both the pressure and the stress gradients Equation (24) can be simplified as

$$\left(\frac{\rho}{\Delta t} \mathbf{M} + \theta \mathbf{K}_{\mathbf{u}} - \theta \mathbf{K}_u^{\Gamma} \right) (\bar{\mathbf{u}}^* - \bar{\mathbf{u}}^n) = -\rho \mathbf{C} \bar{\mathbf{u}}^n - \mathbf{K}_{\mathbf{u}} \bar{\mathbf{u}}^n + \mathbf{L}^{\mathrm{T}} \bar{\mathbf{p}}^n + \mathbf{f}_s - \rho \frac{\Delta t}{2} (\mathbf{C}_1 - \mathbf{C}_2) \bar{\mathbf{u}}^n \tag{33}$$

The iterative procedure described in the last section is applied for the solutions of Equations (33), (25), (26) after the spatial discretization stated as follows:

(1) Let $\bar{\mathbf{u}}_0^{n+1} = \bar{\mathbf{u}}^n$ and the number of iterations $i \Leftarrow 1$.
(2) Compute $\bar{\mathbf{u}}_i^{n+1/2} = (\bar{\mathbf{u}}_{i-1}^{n+1} + \bar{\mathbf{u}}^n)/2$ and use it to solve for $\bar{\mathbf{u}}_i^*$ by Equation (33).
(3) Determine $\Delta \bar{\mathbf{p}}_i$ by the solution of Equations (25) and obtain $\bar{\mathbf{p}}_i^{n+1} = \bar{\mathbf{p}}^n + \Delta \bar{\mathbf{p}}_i$.
(4) Solve Equation (26) to determine $\bar{\mathbf{u}}_i^{n+1}$ by using $\bar{\mathbf{u}}_i^*$ and $\Delta \bar{\mathbf{p}}_i$.
(5) Check for convergence of the ith iteration, if $\|\bar{\mathbf{u}}_i^{n+1} - \bar{\mathbf{u}}_{i-1}^{n+1}\|_{\infty} \leqslant \varepsilon$, terminate the iteration loop, otherwise $i \Leftarrow i + 1$ and go to (2).

4. NUMERICAL RESULTS

4.1. Plane Poisseuille flow problem

The plane Poisseuille flow problem, as shown in Figure 1(a), is solved at different Reynolds numbers ranging from low to high viscosities to compare the performances of the proposed

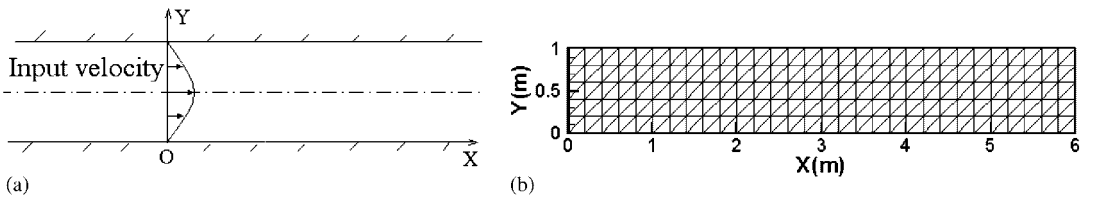

Figure 1. The plane Poisseuille flow problem: (a) schematic diagram; and (b) mesh plot ($h = 0.2$ m).

two iterative versions I-CBS and I-TGBS of the stabilized fractional step algorithm with the existing versions CBS-NE, CBS-IE, TGBS described in Section 2. The transient solutions for the example problem are regarded as a device to obtain the steady state solution. Non-equal order interpolation elements, i.e. T6P3 triangle elements with 6 noded quadratic interpolations for the velocities and 3 noded linear interpolation for the pressure are used. The parameter $\theta = 0.8$ is used for the semi-implicit versions TGBS, I-TGBS and I-CBS.

The geometry of the problem along with the element mesh is shown in Figures 1(a) and (b). No slip conditions are prescribed at the solid wall boundaries, i.e. the fluid is assumed to stick itself to the boundaries and thus all velocity components on the boundaries $u_x = u_y = 0$. The tractions are prescribed to be zero at the exit of the mould cavity. For the plane Poisseuille flow problem $u_y = 0$ and hence $\partial u_y/\partial y$ at the exit can be assumed, with which the incompressibility condition and the traction free condition at the exit lead to $p = 0$ there. The velocity components at the entry boundary are prescribed as $u_y = 0$ and $u_x(0, y) = \alpha y(Y_0 - y)$ with a parabolic distribution along the line $x = 0$, in which α is the coefficient to normalize the fluid flux equal to unit at the entry, Y_0 is the height of the cavity. The theoretical solution for the pressure of the steady state Poisseuille flow problem can be written as

$$p = 2\mu\alpha(X_0 - x) \tag{34}$$

where X_0 is the length of the cavity. The accuracy of the numerical solution for the problem is measured by the relative error defined as

$$\eta = \frac{1}{n+1}\sum_{i=0}^{n}\frac{|p_i^{\mathrm{T}} - p_i^{\mathrm{C}}|}{p_i^{\mathrm{T}}} \times 100\% \tag{35}$$

where $n = 5$, p_i^{T} is the theoretical value of the pressure at $x_i = 0, 1, 2, 3, 4, 5m$ independent of the coordinate y of the point, p_i^{C} is the computational value of the pressure at $x_i = 0, 1, 2, 3, 4, 5m$ determined in such a way that

$$|p_i^{\mathrm{T}} - p_i^{\mathrm{C}}| = \max_{j=0}^{m} |p_i^{\mathrm{T}} - p_{i,j}^{\mathrm{C}}| \tag{36}$$

in which $m = 5$, $j = 0, 1, 2, 3, 4, 5$, $p_{i,j}^{\mathrm{C}} = p^{\mathrm{C}}(x_i, y_j)$, $y_j = 0, 0.2, 0.4, 0.6, 0.8, 1.0m$.

The problem is particularly tested with the three Reynolds numbers, i.e. (1) The flow with the low viscosity and the high Reynolds number ($\mu = 1$ Pa s, $Re = 1000$); (2) The flow with the moderate viscosity and the moderate Reynolds number ($\mu = 100$ Pa s, $Re = 10$); (3) The flow with the high viscosity and the low Reynolds number ($\mu = 2\times10^4$ Pa s, $Re = 5\times10^{-2}$).

Table I. Comparisons of maximum time step sizes $\Delta t_{\max}$(s) taken for different versions of the fractional step algorithm by using T6P3 elements in solutions of the plane Poisseuille flow problem with different Reynolds numbers (in satisfaction of the convergence and the accuracy requirements).

	CBS-NE	CBS-IE	TGBS	I-TGBS	I-CBS
$Re = 1000$	0.03	0.04	Oscillations, hard to converge	Oscillations, hard to converge	0.04
$Re = 10$	0.01	0.01	0.2	1	0.2
$Re = 0.05$	6×10^{-5}	5×10^{-5}	1	1	1

Table I gives the maximum time step sizes allowed to be used for the different versions of the stabilized fractional step algorithm for numerical solutions of the problem with the three different Reynolds numbers under acceptable convergence rate (number of time steps to arrive in a steady state solution) and accuracy (the relative error $\eta \leqslant 5\%$). It is observed that the two proposed iterative versions I-CBS and I-TGBS perform much better in numerical solutions of the problem with the high and the moderate viscosities than the existing explicit versions CBS-NE and CBS-IE. It is noted that the effects of the iterative procedure introduced into the algorithm can be shown by a comparison of the maximum time step sizes required to TGBS and I-TGBS versions at the problem with the moderate viscosity, i.e. the maximum time step size for the version I-TGBS is five times larger than that for the version TGBS. On the other hand, the proposed iterative version I-CBS has much better performance in numerical solutions of the problem with the low viscosity than the existing semi-implicit version TGBS, for which the transient solutions do not converge to a steady state solution even after a huge number of time steps and the node-to-node oscillations of the pressure field appear.

It is noted that both explicit versions CBS-NE and CBS-IE require so small values of $\Delta t_{\max}$ in numerical solutions of the problem with the high and the moderate viscosities and both versions TGBS and I-TGBS do not work in numerical solutions of the problem with the low viscosity, respectively. Hence, those versions cannot be accepted in corresponding cases. In summary the proposed I-CBS version has a better overall performance than others in numerical solutions of the problem with different Reynolds numbers ranging from low to high viscosities.

The plane Poisseuille flow problem with the three different viscosities is further employed to test the capability of the two proposed iterative versions I-CBS and I-TGBS, in comparison with the existing versions CBS-NE, CBS-IE, TGBS, in circumventing the restriction imposed by the LBB condition as the interpolation approximations of the same low order for $\mathbf{u}$–p variables, i.e. T3P3 type elements, are used. Here $\theta = 0.5$ is used for the semi-implicit versions TGBS, I-TGBS and I-CBS.

The study of Guermond *et al.* [6] indicated that the fractional step algorithm can circumvent the restriction imposed by the LBB condition in using the same low order interpolation element T3P3 only provided the non-incremental version of the algorithm is used with the time step size larger than a critical value satisfying $\Delta t \geqslant ch^{l+1}$, in which h is typical size of the element, l the order of interpolation for $\mathbf{u}$–p variables, c the parameter depending on the material property data and the intrinsic characters of the problem in hand. According to the conclusions stated by Guermond *et al.* [6], only the version CBS-NE among the five versions

of the algorithm mentioned in this paper may circumvent the restriction imposed by the LBB condition and use T3P3 element as the other versions I-CBS, I-TGBS and CBS-IE, TGBS described above are incremental ones.

The numerical results of the tested problem obtained by using T3P3 elements indicate that

(1) *For the problem with the low viscosity* ($\mu = 1\,\text{Pa s}$, $Re = 1000$): The transient solutions converge to the steady state solution for CBS-NE version as $\Delta t = 0.09\,\text{s}$ is used but with a poor accuracy ($\eta = 21.1\%$), and what is worth, there is a low-grade node-to-node spatial oscillation which occurs in the resulting pressure field near the exit as shown in Figure 2(a). As time step sizes smaller than $\Delta t = 0.09\,\text{s}$ are used the accuracy of the solution is not effectively improved while the oscillations develop. Figure 2(b) shows the development of severe node-to-node oscillations of the pressure field as $\Delta t = 0.01\,\text{s}$ is used.

For I-CBS, I-TGBS and CBS-NE, TGBS versions the transient solutions converge to steady state solutions, respectively, as different time step sizes are used but with severe spatial oscillations of the pressure fields.

(2) *For the problem with the moderate viscosity* ($\mu = 100\,\text{Pa s}$, $Re = 10$): The transient solutions converge to the steady state solution for CBS-NE version with an acceptable accuracy $\eta = 5.0\%$ and a resulting stable pressure field when $\Delta t = 0.01\,\text{s}$ is used. As the time step size decreases the accuracy of the solution is not improved and node-to-node oscillations of the steady state pressure field, as shown in Figure 3(a), appear when $\Delta t = 0.001\,\text{s}$ is used.

Both CBS-IE and I-CBS versions fail to circumvent the restriction imposed by the LBB condition and result in the steady state pressure distributions with node-to-node oscillations. The effect of the iterative procedure introduced into the algorithm is obviously observed through the comparison of the performances in circumventing the restriction between TGBS

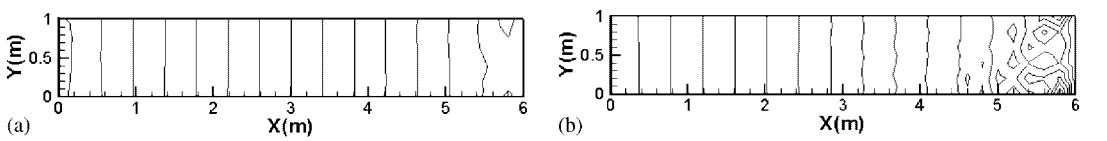

Figure 2. Pressure contours for Poisseuille flow problem ($Re = 1000$) with T3P3 elements: (a) CBS-NE version, $\Delta t = 0.09\,\text{s}$; and (b) CBS-NE version, $\Delta t = 0.01\,\text{s}$.

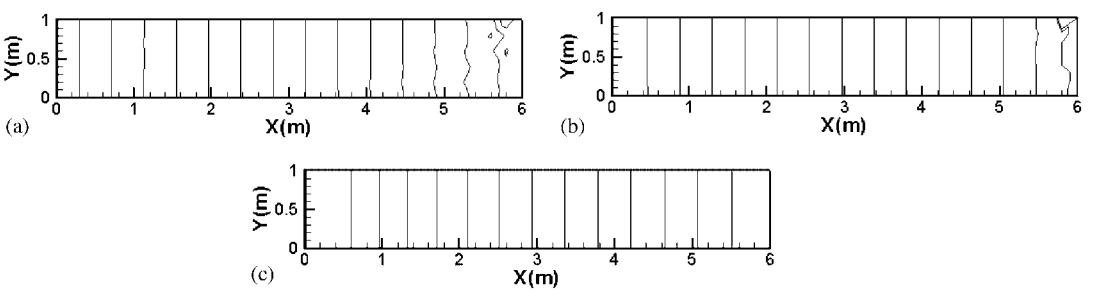

Figure 3. Pressure contours for Poisseuille flow problem ($Re = 10$) with T3P3 elements: (a) CBS-NE version, $\Delta t = 0.001\,\text{s}$; (b) TGBS version, $\Delta t = 1\,s$; and (c) I-TGBS version, $\Delta t = 10\,\text{s}$.

and I-TGBS versions. As the time step sizes $\Delta t > 1$ s are used TGBS version gives stable, converged steady state pressure solutions but with poor accuracies, while $\Delta t = 1$ s is used a converged steady state pressure solution with accuracy $\eta = 5.1\%$ is obtained but slight node-to-node oscillations in the pressure distribution appear as shown by Figure 3(b). In contrast, I-TGBS version gives a stable, converged steady state pressure solution with an acceptable accuracy $\eta = 4.8\%$ as shown by Figure 3(c) when $\Delta t = 10$ s is used. As time step size decreases, corresponding converged steady state pressure solutions remain stable with acceptable accuracies until $\Delta t = 1$ s is used when some extent of node-to-node oscillations of the pressure solution as same as that described above for TGBS version occurs.

The performances of the five versions of the algorithm described above indicate how the minimum time step limitation imposed by the LBB condition effects the application of T3P3 element in the example problem with the low and the moderate viscosities no matter the non-incremental or the incremental versions are used.

(3) *For the problem with the high viscosity* ($\mu = 2\times10^4$ Pa s, $Re = 5\times10^{-2}$): For the version CBS-NE the transient solutions can only converge to a steady state solution with a reluctantly acceptable accuracy $\eta = 5.5\%$ when an unacceptable small time step size $\Delta t = 3\times10^{-4}$ s is used. If one tries to use smaller time step sizes the accuracy cannot be improved, what is worth, node-to-node oscillations of the resulting pressure distribution occur and develop with decreasing time step size. Figure 4(a) shows severe oscillations of the pressure field appearing at the exit as $\Delta t = 1\times10^{-5}$ s is used.

The extremely low value of maximum time step size $\Delta t = 3\times10^{-4}$ s required, which assumedly closes to the minimum time step size limitation imposed by the LBB condition, along with the low accuracy ($\eta = 5.5\%$) of the solution makes the version over low efficient and severely restricts its application for the high viscosity flow problem.

For the version TGBS the transient solutions do not converge to a steady state solution after a huge number of time steps with the step size $\Delta t = 0.2$ s used. As the time step size

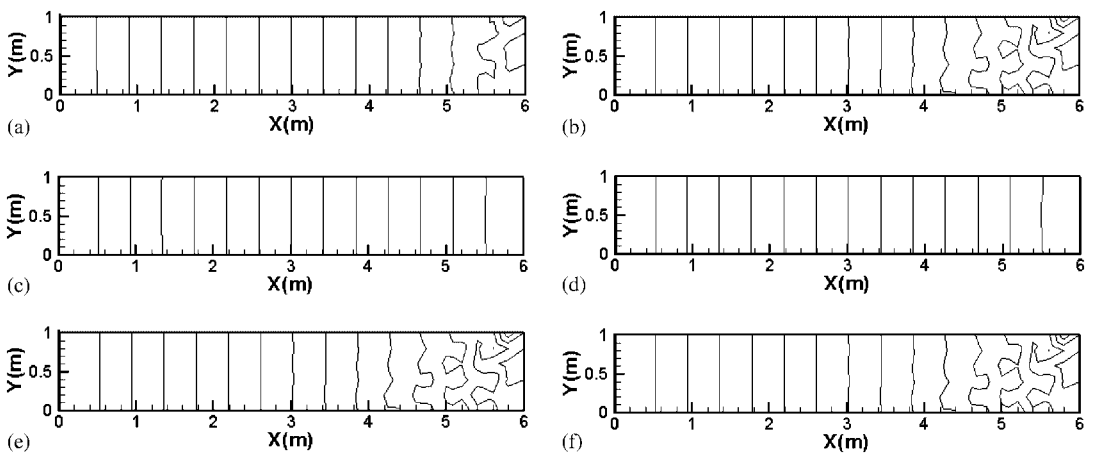

Figure 4. Pressure contours for Poisseuille flow problem ($Re = 5\times10^{-2}$) with T3P3 elements: (a) CBS-NE version, $\Delta t = 1 \times 10^{-5}$ s; (b) TGBS version, $\Delta t = 0.01$ s; (c) I-TGBS version, $\Delta t = 0.5$ s; (d) I-CBS version, $\Delta t = 0.1$ s; (e) I-CBS version, $\Delta t = 0.01$ s; and (f) I-TGBS version, $\Delta t = 0.01$ s.

Table II. Performances of different versions of the fractional step algorithm in circumventing the restriction imposed by the LBB condition as the T3P3 element mesh shown in Figure 1(b) is used for the plane Poisseuille flow problem with different Reynolds numbers.

	CBS-NE	TGBS	I-TGBS	I-CBS
$Re = 1000$	Over large errors or oscillations	Oscillations	Oscillations	Oscillations
$Re = 10$	$0.001\,\mathrm{s} < \Delta t \leqslant 0.01\,\mathrm{s}$ O.K.	Over large errors or oscillations	$1\,\mathrm{s} < \Delta t \leqslant 10\,\mathrm{s}$ O.K.	Oscillations
$Re = 0.05$	$1\times10^{-5}\,\mathrm{s} < \Delta t \leqslant 3\times10^{-4}\,\mathrm{s}$ O.K. (but low accuracy)	Not converge or oscillations	$0.01\,\mathrm{s} < \Delta t \leqslant 0.5\,\mathrm{s}$ O.K.	$0.01\,\mathrm{s} < \Delta t \leqslant 0.1\,\mathrm{s}$ O.K.

decreases, though the convergence is improved but the node-to-node oscillations gradually develop. Figure 4(b) shows the severe oscillations of the pressure field as the time step size decreases to $\Delta t = 0.01\,\mathrm{s}$. In contrast, I-TGBS and I-CBS versions result in the steady state solutions with $\eta = 3.7\%$ and $\eta = 3.4\%$, respectively, at reasonable convergence rates as shown in Figures 4(c) and (d) when quite large time step sizes $\Delta t = 0.5$ and $0.1\,\mathrm{s}$ are used correspondingly. Moreover, as time step size decreases stable steady state solutions with sufficient accuracies still result until it decreases to $\Delta t = 0.01\,\mathrm{s}$ when the node-to-node oscillations appear, as shown in Figures 4(e) and (f) for I-CBS and I-TGBS versions, respectively, due to the effect of minimum time step size limitation imposed by the LBB condition.

Table II summarizes the performances of the proposed iterative versions of the algorithm in comparison with the existing versions CBS-NE and TGBS in circumventing the restriction imposed by the LBB condition as T3P3 elements are used in the example problem. It should be remarked that the conclusions given above by Guermond *et al.* [6] was not fully true, particularly in view of the following facts:

(1) The fractional step algorithm may circumvent the restriction imposed by the LBB condition not only by using the non-incremental versions as indicated by Guermond *et al.* [6] but also by using the incremental versions such as the proposed I-CBS and I-TGBS ones at certain circumstances.
(2) The capability of the different versions of the algorithm in circumventing the restriction is related to the Reynolds number (or the viscosity) of the flow problem in hand. Actually for the present plane Poisseuille flow problem, the non-incremental version CBS-NE is rather reluctant (with low accuracy) in circumventing the restriction in the cases with the moderate and the high viscosities; while the proposed incremental versions I-TGBS and I-CBS are capable of circumventing the restriction in the moderate and the high viscosity cases or in the high viscosity case, respectively, with acceptable accuracies.

4.2. *Lid-driven cavity flow problem*

As the second example a lid-driven cavity flow problem with the cavity sizes $1\times1\,\mathrm{m}^2$ is considered. The enforced boundary conditions for the velocities and the pressure, i.e. $u_x = u_y = 0$ on the boundaries AB, BC, CD, $u_x = 1\,\mathrm{m/s}$, $u_y = 0$ on the boundary AD and $p = 0$ at the

point B, are shown in Figure 5(a). The finite element mesh is plotted in Figure 5(b). The transient solutions for the example problem will converge to a steady state solution.

To demonstrate the performance of the proposed iterative versions of the algorithm in stability, accuracy and efficiency, the lid-driven flow in the cavity is analysed for two different Reynolds numbers, i.e. $Re = 1000$ and $Re = 100$, respectively.

For the case with lower Reynolds number $Re = 100$, the streamlines and the pressure contours at the steady state obtained by using the proposed version I-CBS with the time step size $\Delta t_{\max} = 0.08\,\mathrm{s}$ are illustrated in Figures 6(a) and (b). The shape of the streamlines, the pressure contours and the position (0.61, 0.74) of the eddy centre shown in Figures 6(a) and (b) agree well with the corresponding reference results [11–13], particularly the positions (0.617, 0.734) and (0.617, 0.742) of the eddy centres for the example given by Ghia *et al.* [11] and Schreiber *et al.* [13], respectively.

The time step size $\Delta t_{\max} = 0.1\,\mathrm{s}$ can be taken for the version I-TGBS to run the example and to obtain the results shown in Figures 6(c) and (d), similar to those given in Figures 6(a) and (b) by using the version I-CBS. To indicate the effect of the iterative procedure the example is performed again by using the version TGBS. It is noted that only one half a maximum time step size for I-TGBS, i.e. $\Delta t_{\max} = 0.05\,\mathrm{s}$, can be taken for the version TGBS to obtain the results comparable with those given by the version I-TGBS. It is also pointed that the explicit version CBS-NE requires much smaller time step size $\Delta t_{\max} = 2\times10^{-3}\,\mathrm{s}$ to ensure the stability of the algorithm for running the example. Figure 6(e) shows profiles of the velocity in the u-direction along the centre-line $(0.5, y)$ given by the different versions with similar accuracy, which agree well with the reference results given by Ghia *et al.* [11].

Figures 7(a) and (b) illustrate the streamlines and pressure contours at the steady state for the case with higher Reynolds number $Re = 1000$, obtained by using the proposed version

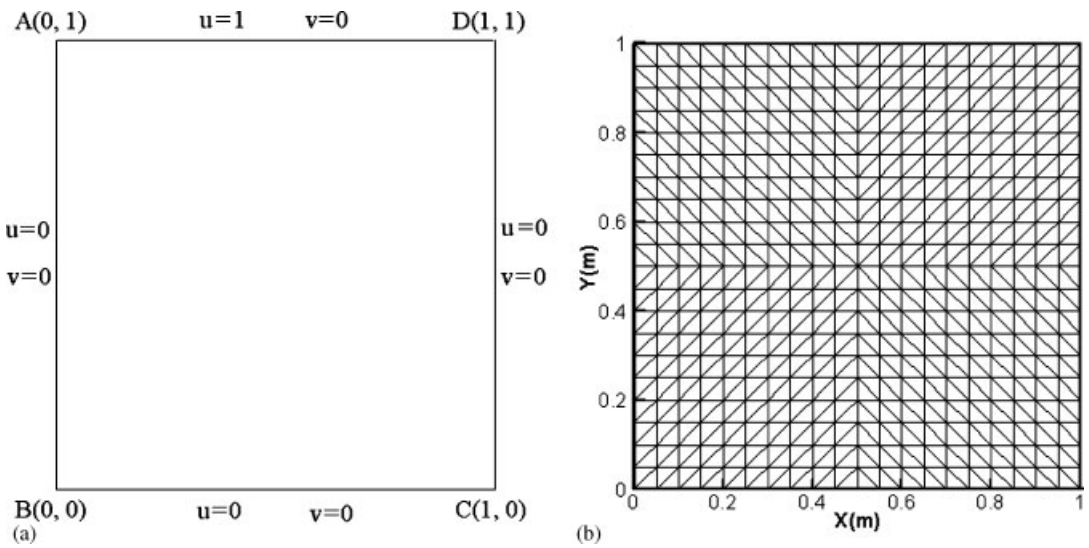

Figure 5. The lid-driven cavity flow problem: (a) geometry and boundary conditions; and (b) mesh plot ($h = 0.05\,\mathrm{m}$).

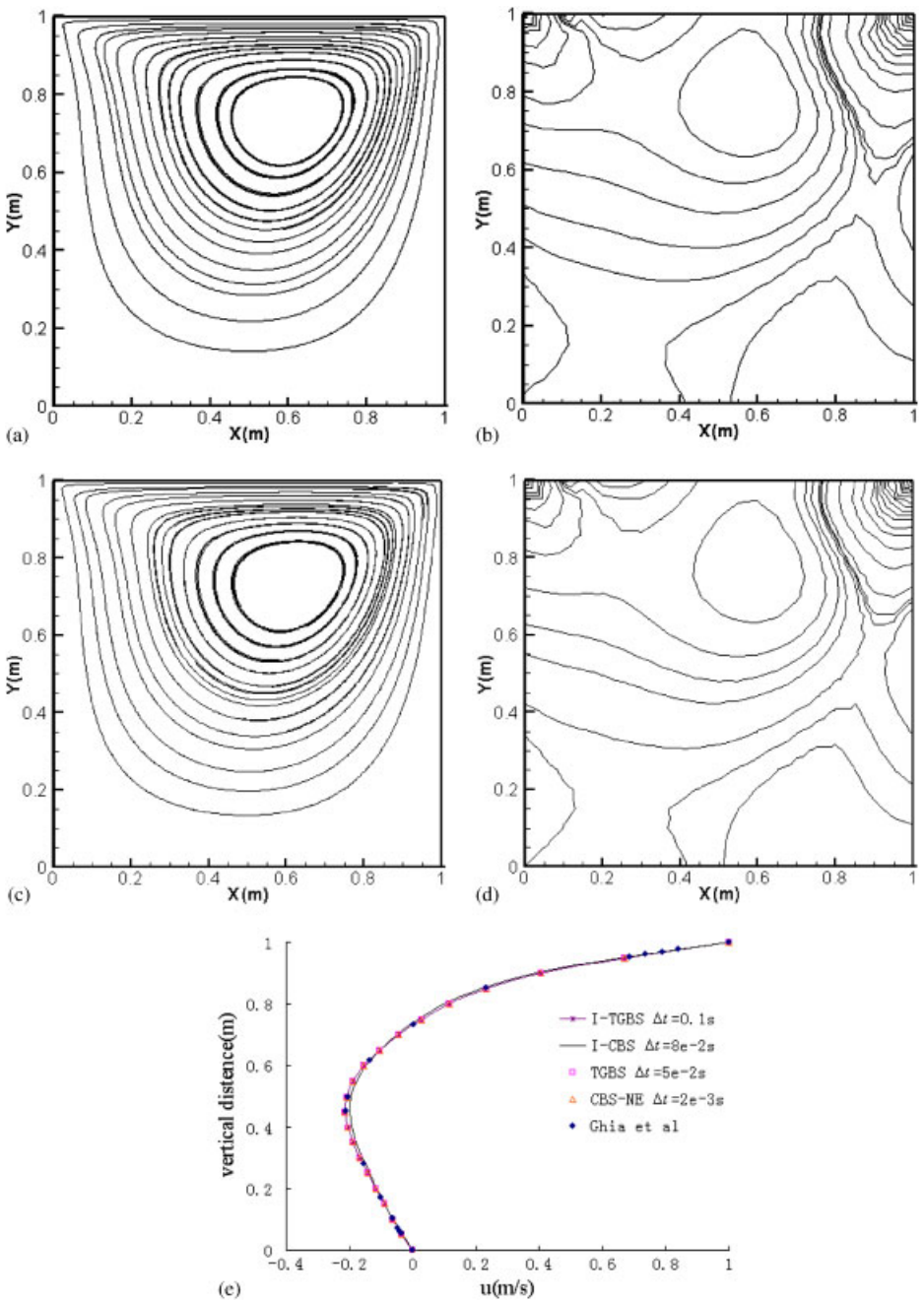

Figure 6. Solutions of the lid-driven cavity flow problem with $Re = 100$: (a) streamlines, I-CBS, $\Delta t = 0.08$ s; (b) pressure contours, I-CBS, $\Delta t = 0.08$ s; (c) streamlines, I-TGBS, $\Delta t = 0.1$ s; (d) pressure contours, I-TGBS, $\Delta t = 0.1$ s; and (e) profiles of the velocity in the u-direction along the centre-line $(0.5, y)$.

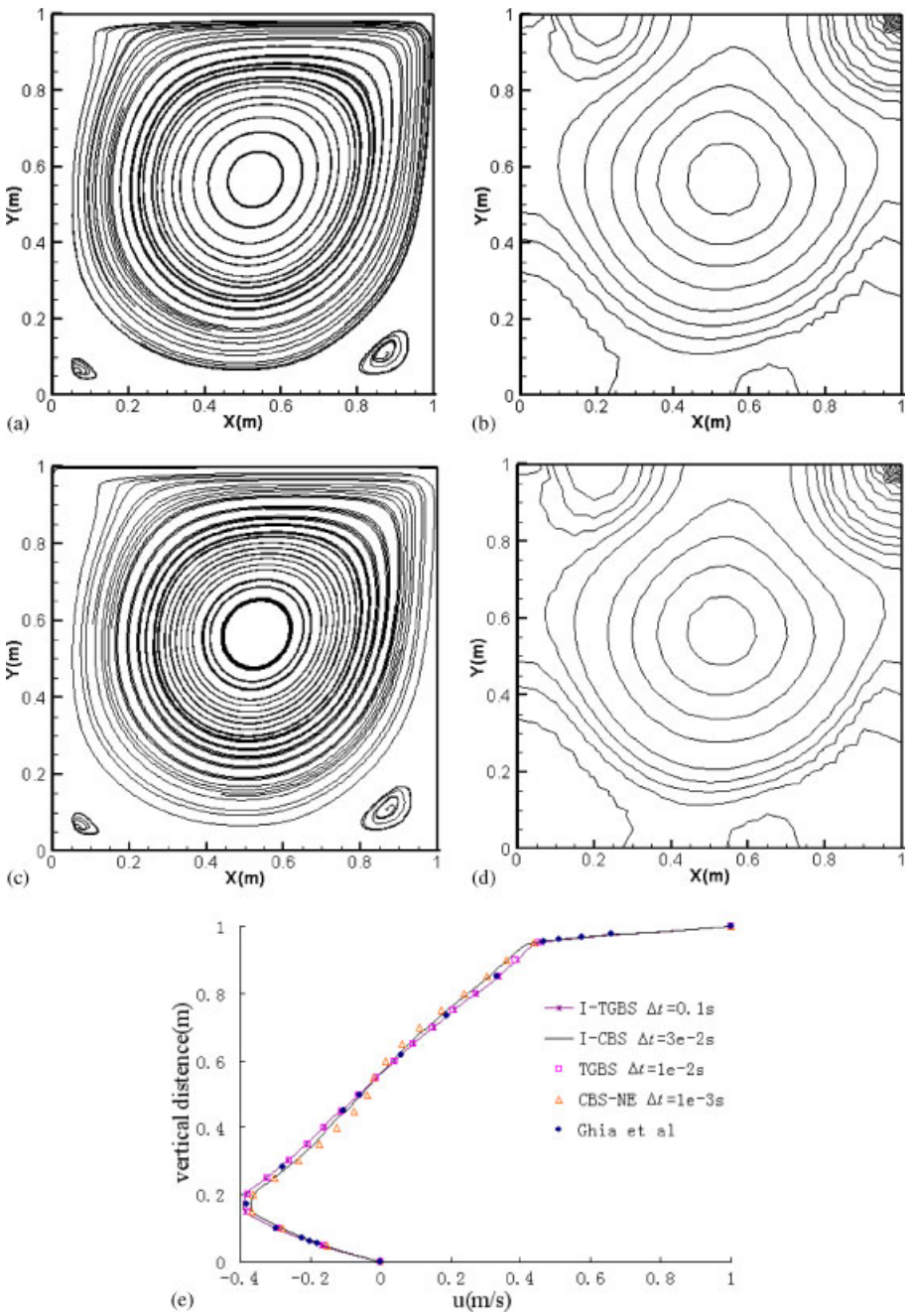

Figure 7. Solutions of the lid-driven cavity flow problem with $Re = 1000$: (a) streamlines, I-CBS, $\Delta t = 0.03$ s; (b) pressure contours, I-CBS, $\Delta t = 0.03$ s; (c) streamlines, I-TGBS, $\Delta t = 0.1$ s; (d) pressure contours, I-TGBS, $\Delta t = 0.1$ s; and (e) profiles of the velocity in the u-direction along the centre-line $(0.5, y)$.

I-CBS with $\Delta t = 0.03$ s. It is observed from Figure 7(a) that the shapes of the three eddies including the so-called primary (P), the first bottom left (BL) and the first bottom right (BR) eddies, the positions of the eddy centres P:(0.53, 0.57), BL:(0.083,0.072), BR:(0.87,0.11) obtained by the proposed version I-CBS agree well with the reference results of Ghia *et al.* [11], in which the positions of eddy centres are given as P:(0.531, 0.563), BL:(0.086,0.078), BR:(0.859,0.109), and the reference results of Schreiber *et al.* [13], in which the positions of eddy centres are given as P:(0.529, 0.564), BL:(0.086,0.071), BR:(0.864,0.107); while the pressure contours illustrated in Figure 7(b) agree well with those, as the reference solutions, given in Reference [9]. Figure 7(c) and (d) give the results obtained by using the version I-TGBS with the time step size up to $\Delta t = 0.1$ s, which are very close to the results illustrated in Figures 7(a) and (b), respectively. In contrast, to obtain the results with the accuracy and the converge rate similar to the results given in Figures 7(c) and (d), a maximum time step size $\Delta t_{\max} = 0.01$ s, one-tenth of the time step size for the version I-TGBS, can be only taken for the version TGBS to run the problem. It is also noted that much smaller maximum time step size $\Delta t_{\max} = 0.001$ s can be only taken for the example as the explicit version CBS-NE is used. Figure 7(e) shows profiles of the velocity in the u-direction along the centre-line $(0.5, y)$ given by the different versions with similar accuracy, which agree well with the reference results given by Ghia *et al.* [11].

4.3. Injection moulding problem

Finally, we apply the proposed version I-CBS of the algorithm to simulate the injection moulding process of the molten polymer.

The geometry of the mould cavity to be filled with the molten polymer is shown in Figure 8. By symmetry, only one half of the mould cavity with the filled molten polymer are taken and discretized. The coordinates of the points which characterize the geometry of the mould cavity are $A(0, 0)$, $B(2.0\,\text{m}, 0)$, $C(2.0\,\text{m}, 2.6\,\text{m})$, $D(3.0\,\text{m}, 2.6\,\text{m})$, $E(3.0\,\text{m}, 3.2\,\text{m})$, $F(1.0\,\text{m}, 3.2\,\text{m})$, $G(1.0\,\text{m}, 1.0\,\text{m})$, $H(0, 1.0\,\text{m})$, as shown in Figure 8. The material parameters of the molten polymer are $\rho = 1000\,\text{kg/m}^3$, $\mu = 2\times10^4$ Pa s. Slip-wall boundary conditions are assumed to simulate wall-slip phenomenon at the solid boundaries, where the shear stress may frequently surpass the critical threshold and fluid slippage at the solid boundaries occurs. The slip coefficient $\beta = 5\times10^{-4}$ s/kg used in Navier's slip condition [14, 15] is assumed to govern

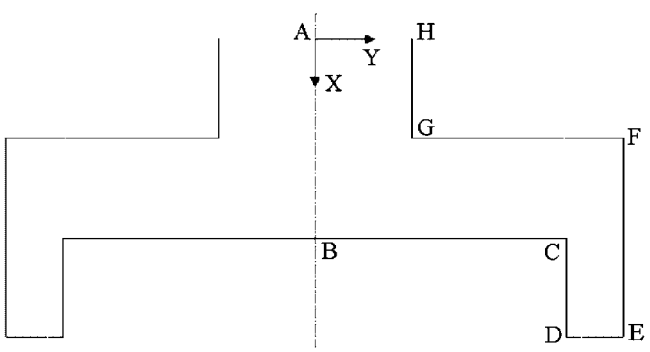

Figure 8. Schematic diagram of a typical filling mould.

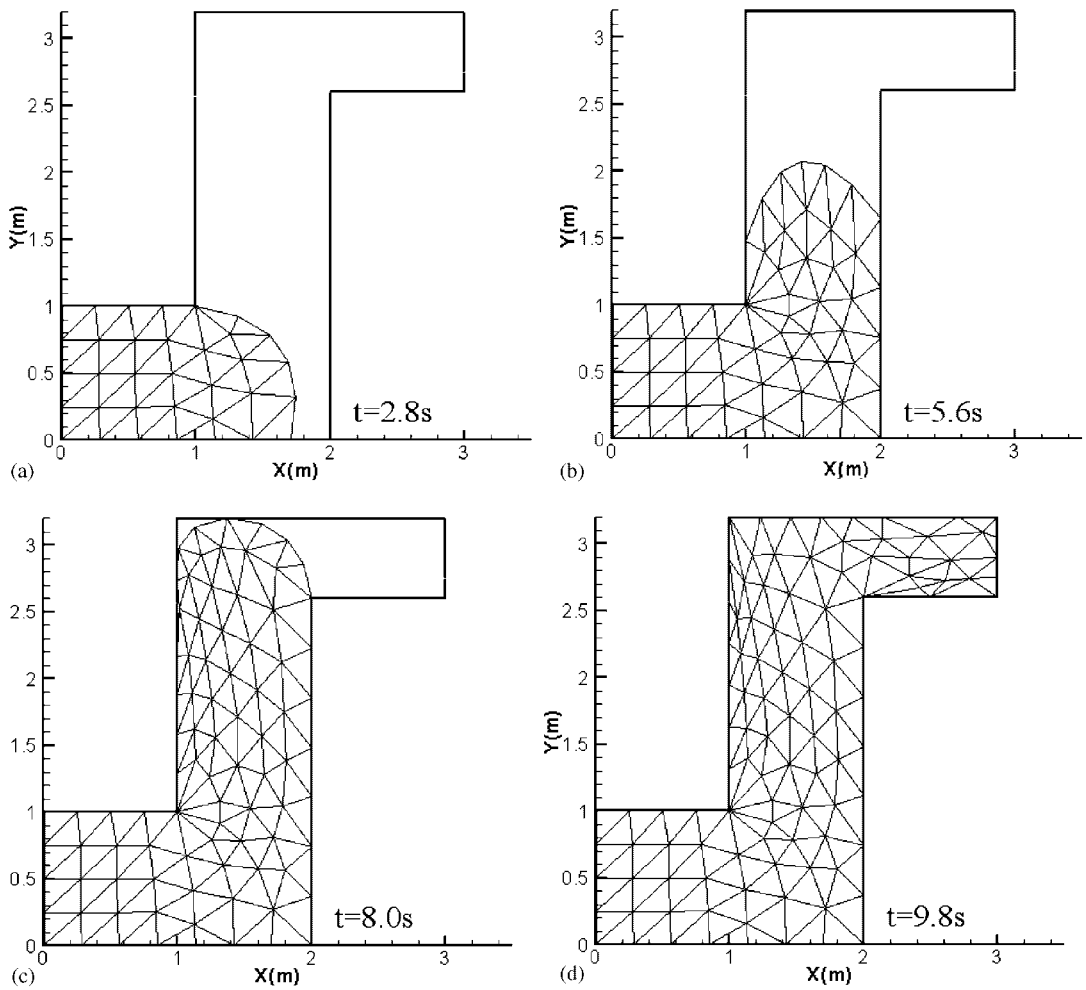

Figure 9. The evolution of the mesh with increasing filled molten polymer mass: (a) $t = 2.8\,\mathrm{s}$; (b) $t = 5.6\,\mathrm{s}$; (c) $t = 8.0\,\mathrm{s}$; and (d) $t = 9.8\,\mathrm{s}$.

fluid slippage of the molten polymer against the solid boundaries. The injection velocities of the molten polymer at the entry of the mould are prescribed as $u_x = 0.5\,\mathrm{m/s}$, $u_y = 0$. T6P3 element mesh updated with the filling process of the molten polymer is used to model the filled polymer domain with time step size $\Delta t = 0.05\,\mathrm{s}$.

The material movement of the molten polymer in the filling process is described by means of the ALE referential configuration with referential particle velocities [16, 17]. The additional equations required to determine the movement of mesh nodes on the free surface is introduced in a self-adaptive manner, which makes it possible to properly capture the moving free surface in numerical simulation of the filling process in different types of complex shaped moulds. The free surface update procedure proceeds according to the movements of the mesh nodes

on the free surface defined as material points and their neighbouring mesh nodes in the filled zone, while the rest of mesh nodes are tackled as the spatial, i.e. the Eulerian, points fixed in the filled zone. Different types of the wall-touching nodes on the free surface are analysed and corresponding schemes to tackle them are developed. The real-time mesh generation of the domain with variable mass of the filled polymer is simplified as a polygon's triangulation in the filled zone near the moving filling front at every given number of time steps. In addition, a local Laplacian smoothing scheme is proposed to improve the mesh quality effectively.

Figures 9–11 illustrates the evolutions of the mesh, the velocity distributions and the pressure contours of the molten polymer domains filled in the mould cavity at the different discrete time levels $t = 2.8, 5.6, 8.0, 9.8$ s. It is observed that the negative pressure region appears in

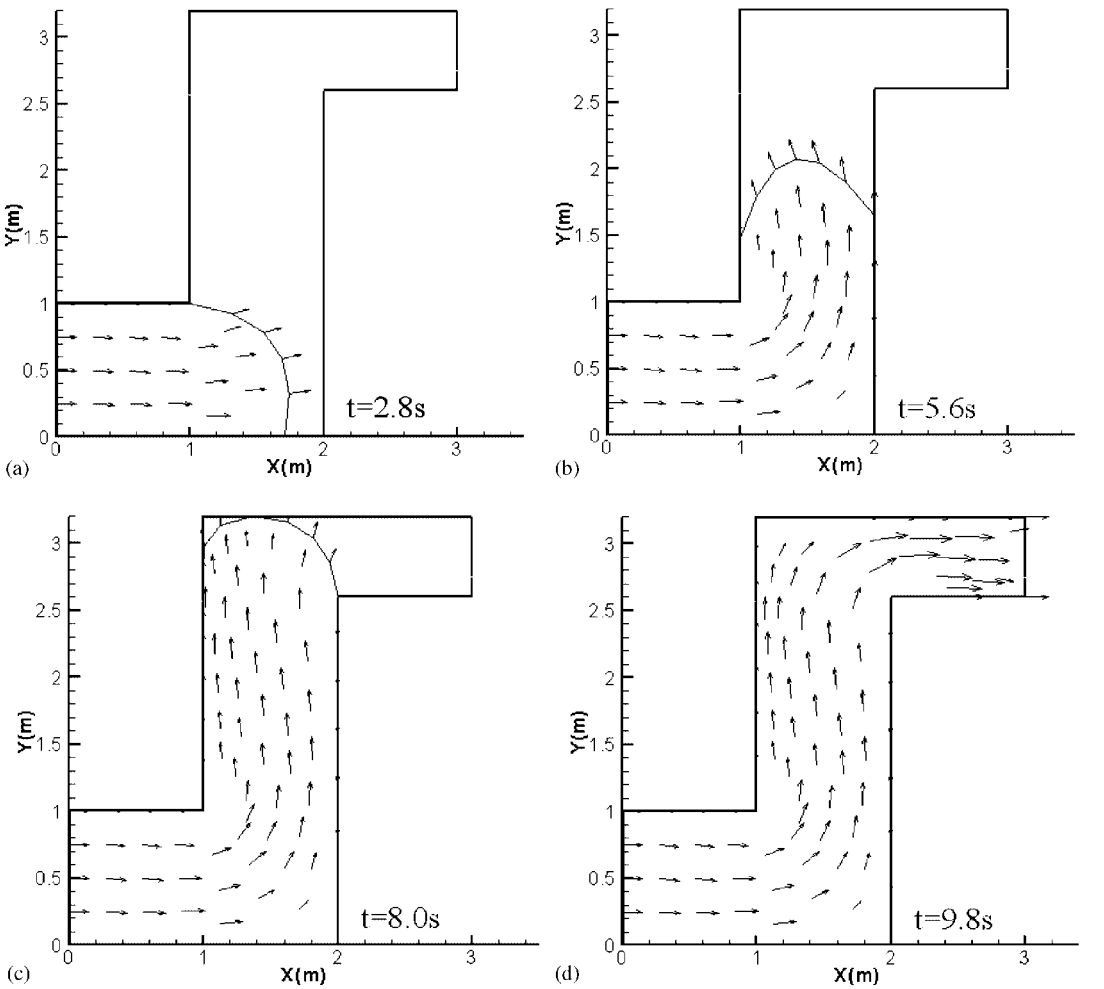

Figure 10. The velocity distributions within the filled molten polymer domains at: (a) $t = 2.8$ s; (b) $t = 5.6$ s; (c) $t = 8.0$ s; and (d) $t = 9.8$ s.

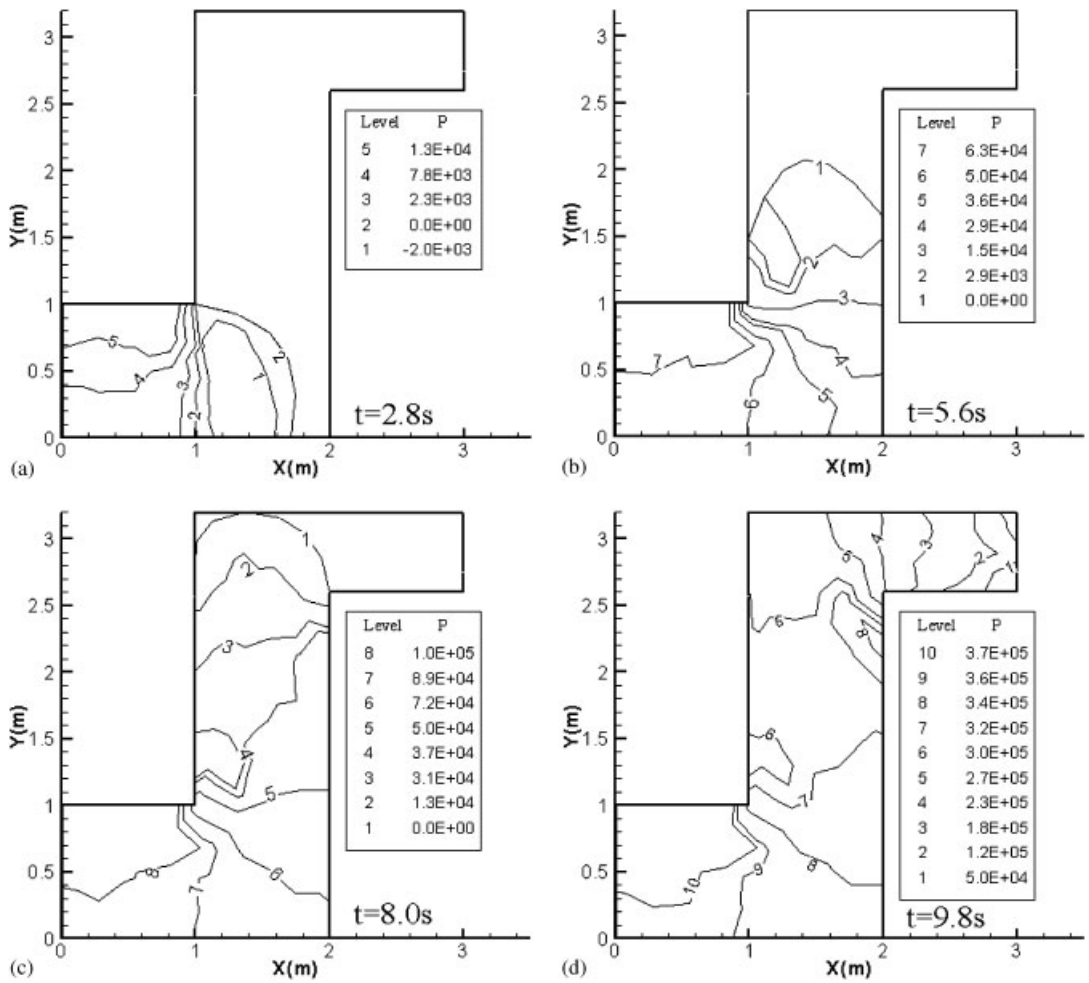

Figure 11. The pressure contours within the filled molten polymer domains at: (a) $t = 2.8$ s; (b) $t = 5.6$ s; (c) $t = 8.0$ s; and (d) $t = 9.8$ s.

Figure 11(a), which means the pressures at the region are less than the datum pressure ($p = 0$) defined to equal the atmosphere pressure 1×10^5 Pa. It can be attributed to the abrupt increase of the cross section at the first corner of the mould, where the transiting melt polymer tends to behave as the expansion like flow that result in the decrease of the pressures at the region. In addition, it is noted that it occurs at the early stage of injection moulding process, when the pressures of the filled melt polymer do not fully develop, that can be explained why the negative pressure region does not occur at the second corner of the mould cavity at the time when the front of the melt polymer passes through there as shown in Figure 11(c).

It is remarked that the proposed I-CBS algorithm allows the time step size $\Delta t = 0.05$ s used for the present example, while the maximum time step size allowed to CBS-NE or CBS-IE

algorithm for the example is only $\Delta t_{\max} = 10^{-4}$ s, which implies more than 10^5 time steps required to take in order to complete the simulation of the injection moulding process of the present example, and prohibits, in fact, the use of the explicit algorithms CBS-NE and CBS-IE in numerical simulations of practical polymer moulding processes.

5. CONCLUSIONS AND DISCUSSIONS

The two versions of the fractional step algorithm are presented in this paper. They are developed on the basis of introduction of an iterative procedure into existing CBS and Taylor–Galerkin (like) based split schemes of the algorithm, respectively, to make the convective terms satisfy temporally semi-discretized equations governing the momentum conservation in the implicit Euler sense. Numerical study fulfilled in this paper indicate that

(1) The introduction of the iterative process into the fractional step algorithm enhances the critical time step size to ensure the stability of the algorithm in general and particularly for the flow problems with moderate and high viscosities. It also makes the incremental (pressure correction) versions of the algorithm, for instance the proposed versions I-CBS and I-TGBS, allow the use of the same low order interpolations for velocity and pressure variables, for instance T3P3 element interpolations, in the flow problems with high viscosities, even both of them were excluded by the study of Guermond *et al.* [6] for justification of using T3P3 type element.
(2) The proposed I-CBS version has a better overall performance in maximum time step size allowed, under comparable convergence rate, stability and accuracy, than other tested versions in numerical solutions of the plane Poisseuille flow and the lid-driven cavity flow problems with different Reynolds numbers ranging from low to high viscosities.
(3) The effect of the iterative process in enhancing the maximum time step size allowed to be taken is particularly indicated by a comparison between the maximum time step sizes for TGBS and I-TGBS versions taken for the flow problems with different viscosities, in which the influence of the convective term to the momentum conservation equation is rather essential.

ACKNOWLEDGEMENTS

The authors are pleased to acknowledge the support of this work by the National Natural Science Foundation of China through contract/grant numbers 10272027, 10590354 and 50278012 and the National Key Basic Research and Development Program (973 Program, No. 2002CB412709).

REFERENCES

1. Chorin AJ. Numerical solution of the Navier–Stokes equations. *Mathematics of Computation* 1968; **22**:742–762.
2. Chorin AJ. On the convergence of discrete approximation to the Navier–Stokes equations. *Mathematics of Computation* 1969; **23**:341–353.
3. Temam R. Sur l' approximation de la solution des équations de Navier–Stokes par la méthode des pas fractionnaries II. *Archives for Rational Mechanics and Analysis* 1969; **33**:377–385.
4. Comini G, Del Guidice S. Finite element solution of incompressible Navier–Stokes equations. *Numerical Heat Transfer*, *Part A* 1972; **5**:463–478.

5. Donea J, Giuliani S, Laval H, Quartapelle L. Finite element solution of unsteady Navier–Stokes equations by a fractional step method. *Computer Methods in Applied Mechecanics and Engineering* 1982; **33**:53–73.
6. Guermond JL, Quartapelle L. On stability and convergence of projection methods based on pressure Poisson equation. *International Journal for Numerical Methods in Fluids* 1998; **26**:1039–1053.
7. Xikui L, Xianhong H, Pastor M. An iterative stabilized fractional step algorithm for finite element analysis in saturated soil dynamics. *Computer Methods in Applied Mechanics and Engineering* 2003; **192**:3845–3859.
8. Zienkiewicz OC, Codina R. A general algorithm for compressible and incompressible flow—part I: The split, characteristic-based scheme. *International Journal for Numerical Methods in Fluids* 1995; **20**:869–885.
9. Zienkiewicz OC, Taylor RL. *The Finite Element Method* (5th edn). Butterworth Heinemann: Stoneham, MA, 2000.
10. Hawken DM, Tamaddon-Jahromi HR, Townsend P, Webster MF. A Taylor–Galerkin-based algorithm for viscous incompressible flow. *International Journal for Numerical Methods in Fluids* 1990; **10**:327–351.
11. Ghia U, Ghia KN, Shin CT. High-Re solutions for incompressible flow using the Navier–Stokes equations and a multigrid method. *Journal of Computational Physics* 1982; **48**:387–411.
12. Shuling H, Qisu Z, Shiyi C, Doolen G, Cogley AC. Simulation of cavity flow by the Lattice Boltzmann method. *Journal of Computational Physics* 1995; **118**:329–347.
13. Schreiber R, Keller HB. Driven cavity flows by efficient numerical techniques. *Journal of Computational Physics* 1983; **49**:310–333.
14. Vahid N. *Practical Aspects of Finite Element Modelling of Polymer Processing*. Wiley: New York, 2001.
15. Silliman WJ, Scriven LE. Separating flow near a static contact line: slip at a wall and shape of a free surface. *Journal of Computational Physics* 1980; **34**:287–313.
16. Xianhong H, Xikui L. An ALE finite element model for the injection molding process. *Chinese Journal of Applied Mechanics* (in Chinese), in press.
17. Xianhong H, Xikui L. A free surface tracking and mesh generation scheme for the injection molding process. *Journal of Dalian University of Technology* (in Chinese), in press.

